Journal of Materials Chemistry C

ROYAL SOCIETY OF CHEMISTRY

PAPER

View Article Online
View Journal | View Issue

Cite this: J. Mater. Chem. C, 2023, 11, 7682

Anisotropic sol–gel transition and morphological aspects of a hierarchical network of nematic gel and a superimposed photopolymer†

G. V. Varshini, D. S. Shankar Rao * and S. Krishna Prasad

Received 20th March 2023,
Accepted 11th May 2023

DOI: 10.1039/d3tc00991b

rsc.li/materials-c

We report investigations on a liquid crystal confined in a hierarchical double network arising from the fibres of an organogelator and a photopolymer. The morphological characteristics and the gel point are seen to be strongly dependent on temperature, or more accurately on the thermodynamic phase in which the polymerization is carried out and also the concentration of the reactive monomer. The presence or absence of the anisotropy of the phase as well as the fluid or the gel character present architectures that are substantially different in complexity as quantified by the fractal dimension obtained from scanning electron microscopy images. The main aspect of this study, which includes dielectric as well as elastic constant measurements, is the attractive feature of hierarchical networks wherein the polymer and gel networks are caused by different chemical species providing a control to have one of them superimposed on the other leading to interesting confined geometry effects.

1. Introduction

Several studies involving the structural,[1–3] morphological, optical, electro-optic, and dielectric properties of liquid crystals (LCs) confined in pre-fabricated or *in situ* created scaffolds have brought to fore the importance of restricted geometry in anisotropic condensed matter systems.[4–9] In this regard, networks created by dopants, such as polymerizable monomers and gelators, have been studied considerably. Physical gels that combine the anisotropic character of LCs and the mechanical rigidity of the thermoreversible network have been reported to present significant consequences on the LC-gel (LCG) properties, faster electro-optic response, anomalous variations in elastic constants, enhanced photoluminescence, and applications in soft robotics and flexible displays.[10–17] We have just reported[15] the novel influence of sample thickness and applied pressure on the characteristics of an organogel exhibiting a nematic-to-nematic-gel transition. It was found that the gelation temperature (T_{sg}) depends strongly on the sample thickness d, for $d < 30$ μm. On the other hand, applied pressure hinders the gelation process, resulting in a reduced thermal range of the nematic-gel phase. In light of these fascinating findings, we now describe a new dimension to the LCG systems in the form of another constraint played by polymer confinement in the presence or absence of a second network due to gelation, thus mimicking a hierarchical network.

Polymer-modified LC systems are well known for applications, such as privacy windows, switchable THz devices, electro-optic devices, and optical filters.[4,16–21] Depending on the polymer content in the LC medium, they can be of two types: polymer dispersed liquid crystals (PDLCs) and polymer stabilized liquid crystals (PSLCs). While the former is polymer-rich, in the latter case, the polymer is a minority component. A judicious balance of the material content and the refractive index difference between the polymer and LC gives rise to various modifications in LC properties, such as lowered operating voltages, better scattering ability, and reduction in the backflow effect,[22–24] which are essential for device applications.

To understand the polymer + LC network characteristics in liquid, LC, and LC gel environments, we investigated a system wherein the network formation of the gel occurs independent of the monomers that get polymerized. We realised that these systems may be viewed as a parallel amalgamation to the double or inter-penetrating networks, well-studied in hydrogels and polymer gel systems.[26–34] Such networks, especially in hydrogels, can be formed either by utilizing polymers or low molecular weight organogels. For instance, two orders of magnitude higher (from 0.2 MPa to 25 MPa) sustainability to compression stress was observed in a double network hydrogel system compared to its single network counterpart,[25] even when the water content was nearly 90%. Another example mimicked the extra-cellular matrix for tissue formation and regeneration.[26–28] These and such observations have opened up

Centre for Nano and Soft Matter Sciences, Shivanapura, Bangalore, 562162, India. E-mail: raoshankards@gmail.com

† Electronic supplementary information (ESI) available. See DOI: https://doi.org/10.1039/d3tc00991b

possibilities to deploy them in drug delivery systems, tissue engineering, biosensors, soft contact lens, *etc.*[29–33] Extension of competing network strategy studies to an anisotropic environment will add another dimension to the knowledge base on two networks imposed on a single host.

Although there have been no reports of including two networks in a liquid crystal host, Kato *et al.*,[34] investigated a photopolymerisable gelator system that displayed enhanced electro-optical responses. Even if one considers this system to have two networks, each of polymerization and gelation, the aspect that the same material leads to both mechanisms reduces the extent of tunability and sequential aspects. Hence, this study is the first of its kind, wherein the two physical networks are caused in a hierarchical fashion by two different materials added to the liquid crystal host. Apart from the fact that we are exploring a new direction, it is observed that the thermodynamic phase of the system offers itself as a parameter for controlling the morphology of the network. For this purpose, we employed a photo-polymerizable monomer and a low-molecular-weight organogelator as separate entities and carried out the polymerization at different temperatures or rather in different phases. This protocol exploits the fact that polymer networks formed mimic, to a great extent, the orientation of LC molecules during polymerisation.[4,16,35] We have analysed the details of the morphology of the polymer strands formed, voids created due to the LC trapped within the polymer networks, the mutual interaction of the two networks involved, and their impact on other liquid crystal properties such as gelation and elastic constants based on their hierarchy of existence.

2. Experimental methods

2.1 Materials used and sample preparation

The host LC material (labelled TCMG) consists of a three-LC component mixture and a low-molecular-weight organogelator, 12-hydroxystearic acid, (HSA), present at a concentration of 1.5 weight%. TCMG exhibits the nematic phase over a wide temperature range from 54.2 °C to sub-ambient temperatures as confirmed by polarising optical microscope (POM). A diacrylate reactive mesogenic monomer (RM82 from Merck), added at different concentrations to TCMG, served as the photo-polymerizable monomer. The polymerization was initiated by adding a small amount (2% of RM82) of photoinitiator (BME, Aldrich). The molecular structures of the employed materials and their transition temperatures are shown in Fig. S1(a)–(d) (ESI†). For preparing the polymerizable mixture, required amounts of TCMG, RM82, and BME were weighed and mixed physically at $T \sim 120$ °C, well above the isotropic temperature of TCMG.

To understand the mutual influence of polymer and gel networks in detail, we studied seven different concentrations of RM82 in TCMG: X_{RM} = 0.5, 1, 1.25, 1.5, 1.75, 2, and 3, where X_{RM} denotes the weight% of RM82 in TCMG. The phase sequence of TCMG remains unaltered upon the addition of RM82, over the range of concentrations studied. All the composites studied show the phase sequence isotropic (Iso) → nematic sol (N_{sol}) → nematic gel (N_{gel}) on lowering the temperature. TCMG + monomer mixtures were filled into the cells, whose thickness was maintained around 12–15 μm, using capillary action well above the isotropic temperature. For orienting the nematic director in the planar fashion, the substrates forming the cell were treated with a unidirectionally rubbed polyimide layer. Polymerization of the samples was carried out with low-power (3 mW cm^{-2}) UV radiation having a peak wavelength of 365 nm.

As discussed in the introduction, the primary focus of these studies was to explore the influence of the order of the mesophase on the morphology of the networks formed and on the gelation properties. Hence, the filled cells, labelled as G-P, N-P, and I-P and were polymerized in the three different phases – (a) at 30 °C in the gel phase, (b) at 50 °C in the nematic phase, and (c) at 60 °C in the isotropic phase. This process enabled us to examine the effect of LC orientation at different levels on the network formation and in turn the influence of the first gel/polymer formed network on the second polymer/gel network.

2.2 Measurement techniques

Field emission scanning electron microscopy (FESEM). Detailed morphological analyses of the polymer strands were performed by FESEM using the MIRA 3 LHU (Tescan and Bruker) instrument. For this purpose, after polymerization, the cells were immersed in a suitable solvent for 12 hours so that the unpolymerized content, LC + gelator, was removed leaving only the polymer network on the substrate. The cells were opened carefully without disturbing the RM82 strands and the substrates were subjected to imaging.

Haze measurements. Haze, an important factor for scattering/transparency-based devices and defined as the total transmittance of light through a material, is dependent on the amount of visible light diffused or scattered. Thus, the lower the haze value, the higher the transparency of the sample. A simple transmittance spectrum in different conditions provides the required data to calculate the haze factor using the expression,

$$\text{Haze}\,(\%) = \left(\frac{T_4}{T_2} - \frac{T_3}{T_1}\right) \times 100 \qquad (1)$$

Here, T_1–T_4 are the transmitted intensities measured using an integrating sphere detector under the following conditions: T_1, no sample, but only the standard white reflector at the back; T_2, sample in front and reflector at the back; T_3, no sample, no reflector; and T_4, only sample (see Fig. S2, ESI†). Under these conditions, the measured haze is 0% for a perfectly transparent sample and 100% for a perfect white diffuser (also known as white standard). The measurements of T_1–T_4 were carried out on selected samples using a UV-visible spectrometer (PerkinElmer – Lambda 750) fitted with an integrating sphere detector covering the wavelength range 400–800 nm, and the haze was determined using eqn (1).

Electrical behaviour. Sample capacitance measurements were performed to understand the dielectric behaviour as well as to determine the splay (K_{11}) Frank elastic constant through

electric field-driven Freedericksz transition. Upon application of the field normal to the substrate, above a certain threshold voltage (V_{th}), the molecules will reorient from their equilibrium planar alignment and achieve homeotropic orientation in the limiting case. This reorientation of the molecules from planar to homeotropic can also be utilised to analyse the switching dynamics of the system. The electro-optical switching of the samples was studied by monitoring the transmitted intensity through the POM while applying an electrical field. The transmitted light from the sample was collected using a photo-diode, the output of which was fed to an oscilloscope (PicoScope 4262). This signal was further analysed to obtain the response timescales of the material.

3. Results and discussions

The studied system involves both polymer and gel networks formed on a hierarchical basis that arises owing to the temperature (or equivalently the mesophase) at which the polymerization is carried out. The characteristics of this dual network on the G-P, N-P and I-P samples for different compositions (X_{RM}) of the RM material are comprehended from three different viewpoints: (a) morphological aspects, (b) effect on the gelation temperature and (c) dielectric behaviour.

3.1 Morphological observations

Polarising optical microscope studies. We begin to look at the morphological aspects of the polymer networks at a coarse level through POM images and elucidate in detail through SEM images discussed in the next section. The formed polymer networks were visualised under POM in the isotropic phase to avoid the contribution from the birefringence of the nematic phase; the residual birefringence of the polymer provides a good contrast. As we carried out a detailed study of varied monomer concentrations and their polymerization in three different phases, networking with each X_{RM} is distinct in its own way. The orientation of the polymer network formed is dictated by the LC director's orientation in the surrounding environment. An additional feature that should be emphasized is that RM82 itself exhibits a nematic state in its monomeric form. In contrast, the gelator HSA molecules, without an aromatic moiety, do not show the nematic phase. Still, the orientational order of the neighbourhood may still impose such an order on the HSA molecules, albeit with a smaller magnitude. However, mere orientational order may not ensure that the hydroxy/carboxyloxy groups of neighbouring HSA molecules are in a favourable position for hydrogen bonding, which would certainly have a bearing on gelation. With this background, we shall proceed further to discuss the network formation and related properties in G-P, N-P, and I-P samples. For low (<1.5) X_{RM} concentrations, the scarcity of the monomer units results in incomplete network formation wherein the unconnected droplets are observed. For $X_{RM} > 1.5$, well-connected networks are seen with the density of fibres increasing as X_{RM} increases. This common trend is exhibited by all G-P and N-P samples, as shown in Fig. 1 and 2, respectively. The influence of the nematic orientation in achieving an aligned polymer network is evident in Fig. 2. Despite the aligned networks seen in both N-P and G-P cases, there are certain contrasting features also,

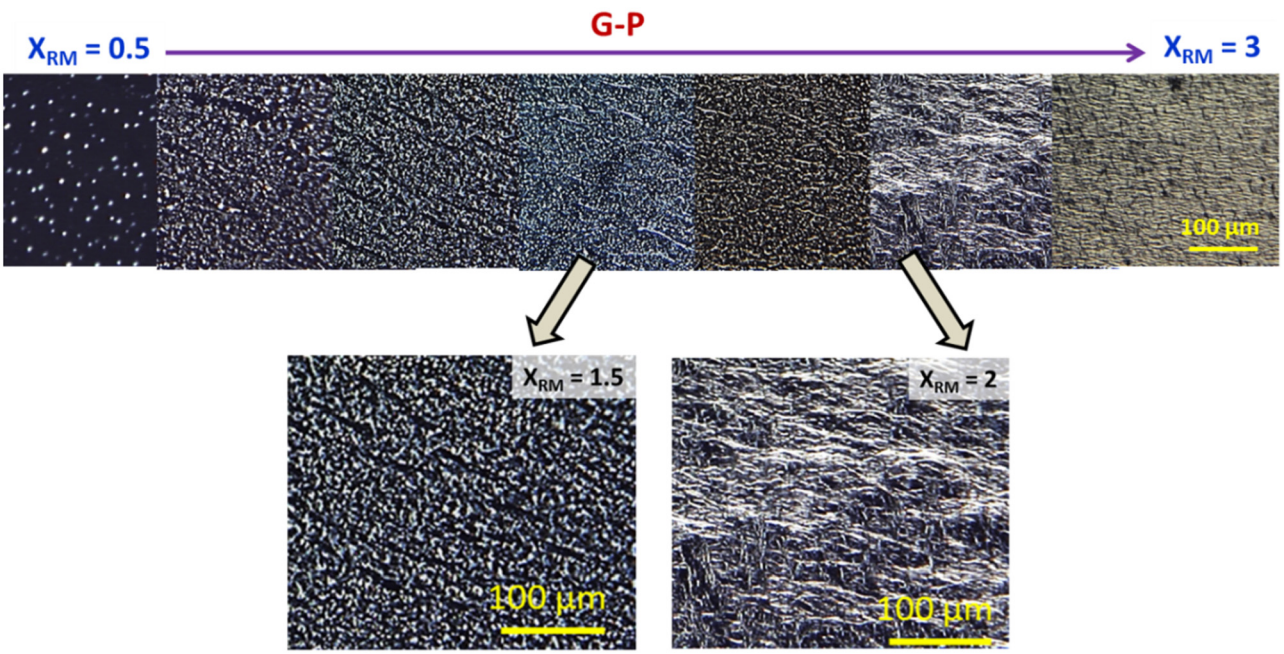

Fig. 1 POM images taken in the isotropic for samples polymerised in gel phase (G-P) with varied concentrations of photopolymer (X_{RM}). Droplet morphology was seen for lower X_{RM}, and improved the connectivity of the polymer strands was observed with the increase in the monomer concentration. Although enlarged images (below) display well-connected polymer networks at higher X_{RM}, the networks are more distorted; a consequence of the surrounding nematic-gel environment.

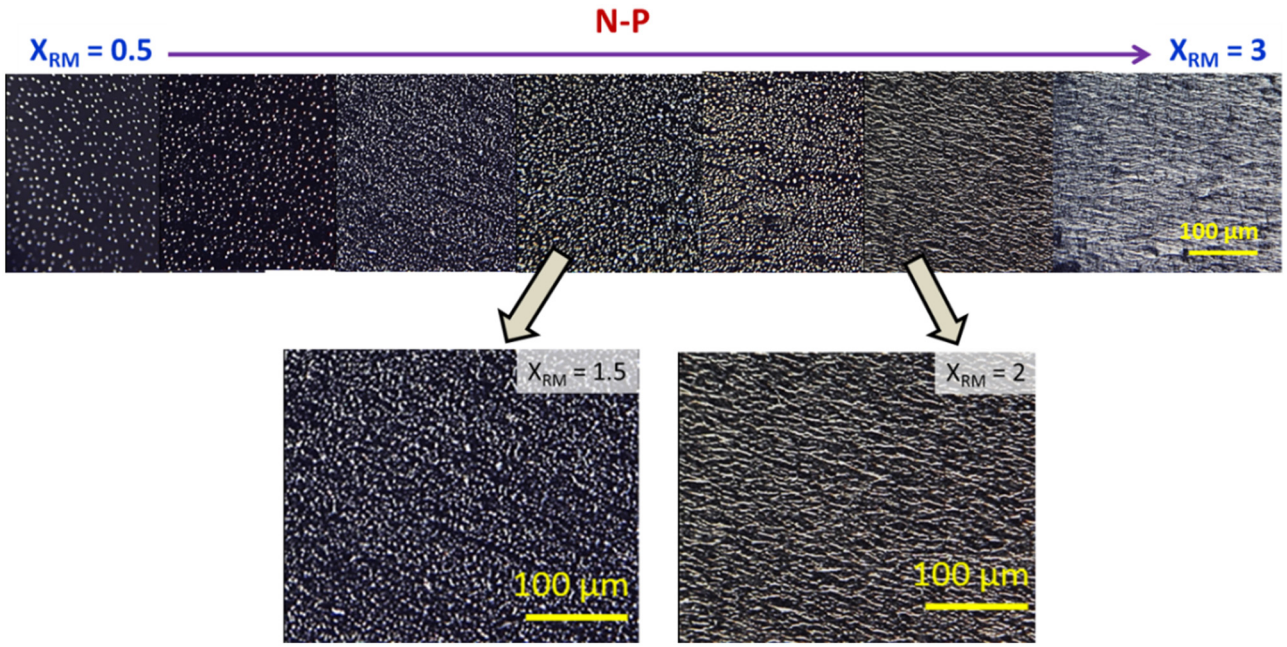

Fig. 2 POM images taken in the isotropic for samples polymerised in the nematic phase (N-P) for varied X_{RM}. While droplet morphology is seen for lower X_{RM}, as the monomer concentration increases, improved connectivity of the polymer fibres was observed. Enlarged images (below) display oriented polymer strands that are the resultant of the surrounding aligned nematic environment.

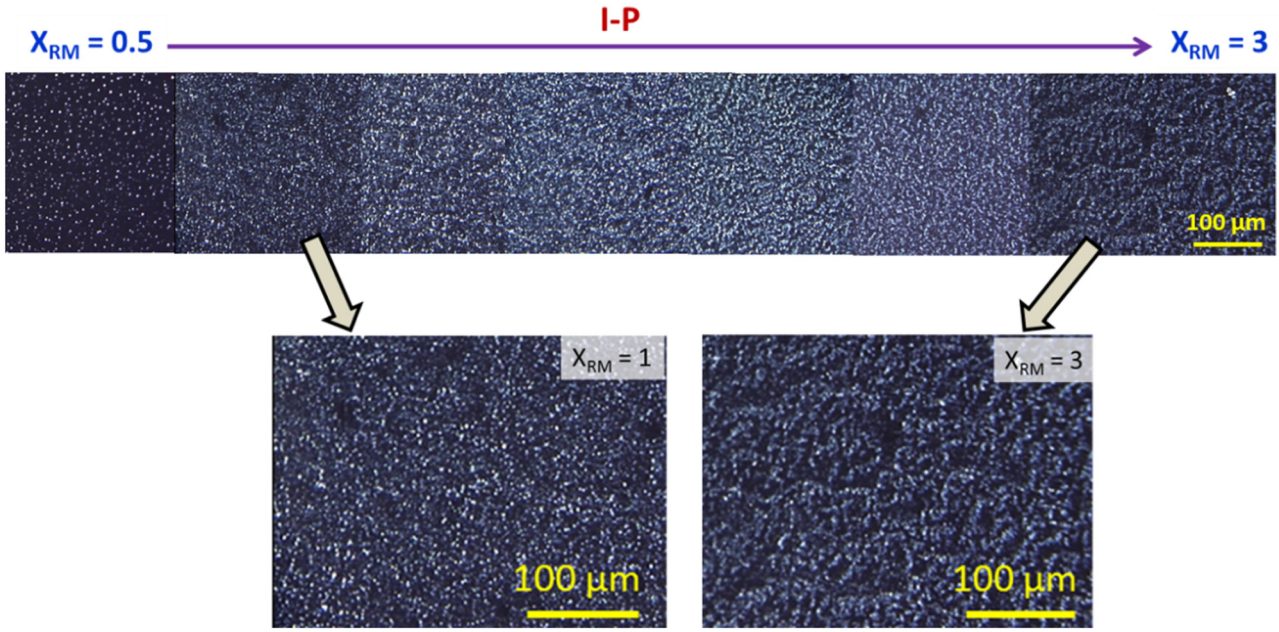

Fig. 3 POM images taken in the isotropic when polymerised in the isotropic phase (I-P) for varied X_{RM}. No connected strands are observed for any X_{RM}, even in enlarged images (shown below).

arising primarily due to the fact that when the sample is polymerised in the gel phase, there is already an underlying (gel) network in the system. As mentioned earlier, during gelation, there is no direct control on the hydrogen bonding of the HSA molecules, a fact that reflects in the observation of the disoriented polymer strands seen in Fig. 1, more so at higher X_{RM}. The power of the orientational order in the morphological aspect of the network is evident from the images in Fig. 1 and 2 (G-P and N-P cases) comparing with those in Fig. 3 obtained for the I-P samples; no concentration of RM studied exhibited network formation.

Thus, achieving oriented networks seem to be requiring the orientation of HSA molecules as well. In addition, if a molecular-level control can be realized wherein the H-bondable units of

neighbouring HSA molecules are placed in favourable positions, then even better-oriented hierarchical networks can be expected. The strength of the gel network overseen by the concentration of HSA could bring an additional control parameter.

SEM images and analyses. After POM imaging, the same sample cells were imaged by SEM imaging after subjecting them to the procedure already described in Section 2.2. Briefly, first, the TCMG host was leached out by immersing the cells in a suitable solvent. Once the LC was completely removed, the cells were opened up to expose the formed network, and to have high contrast, a thin layer of gold was sputtered onto the network. Fig. 4 shows the SEM images for X_{RM} = 3 for all three, G-P, N-P, and I-P cases.

In consonance with the observations under POM, excellent spatially continuous networks are seen for the nematic and gel polymerized samples, but not for the isotropic case. Careful observations of these images reveal the contrasting behaviour between the N-P and G-P samples with the former having director-dictated far better orientation than their counterpart gel polymerized (G-P) sample affected by the random orientation due to the existing gel network and its influence on the yet to be polymerised monomer units. The regions enclosed by the polymer network creating void-like structures are similar to those reported in hydrogels presenting an interpenetrating network.[36,37] We shall return to this point later.

We now compare the situations for two different monomer concentrations, X_{RM} = 1.75 and 3. Unlike the images for the latter material (Fig. 4a–f), the SEM images for lesser monomer concentration (Fig. 5a–d), do not present any noticeable difference in the morphology of the N-P and G-P samples. For example, in the higher concentration material, the G-P case has a much less orientationally ordered structure than the N-P sample, whereas in the X_{RM} = 1.75 system, such an order is essentially retained in the G-P sample also, although with an increased density of fibres (compare Fig. 5(b) and (d)). As expected, the I-P samples of both concentrations, do not exhibit any network formation (see Fig. 4(g–i) and 5(e, f)), albeit showing the presence of randomly oriented short strands, as highlighted in the inset in Fig. 5(f). According to a few studies[38,39] on the gel phase exhibited by polymers, the development of the network begins with the formation of domains, which in turn act as nucleation centres. These discrete nucleation centres intersect as they grow and tend to form a network of self-assembled polymers strands.[38] Obviously, the higher the

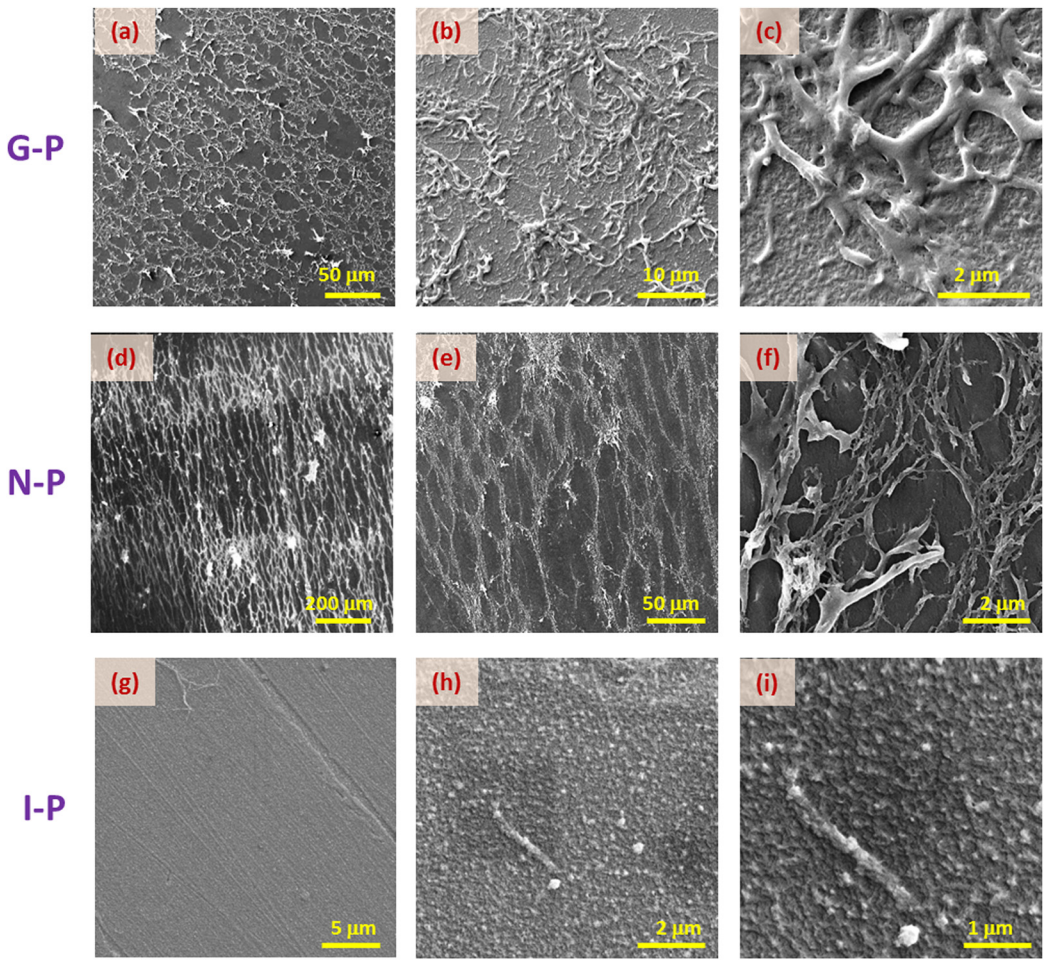

Fig. 4 SEM images depicting the polymer networks for X_{RM} = 3 with magnifications of (a) 0.5 × 10^3, (b) 3 × 10^3, (c) 20 × 10^3, (d) 0.125 × 10^3, (e) 0.5 × 10^3, (f) 15 × 10^3, (g) 5 × 10^3, (h) 15 × 10^3, (i) 30 × 10^3 for G-P, N-P and I-P samples shown from top to bottom, respectively.

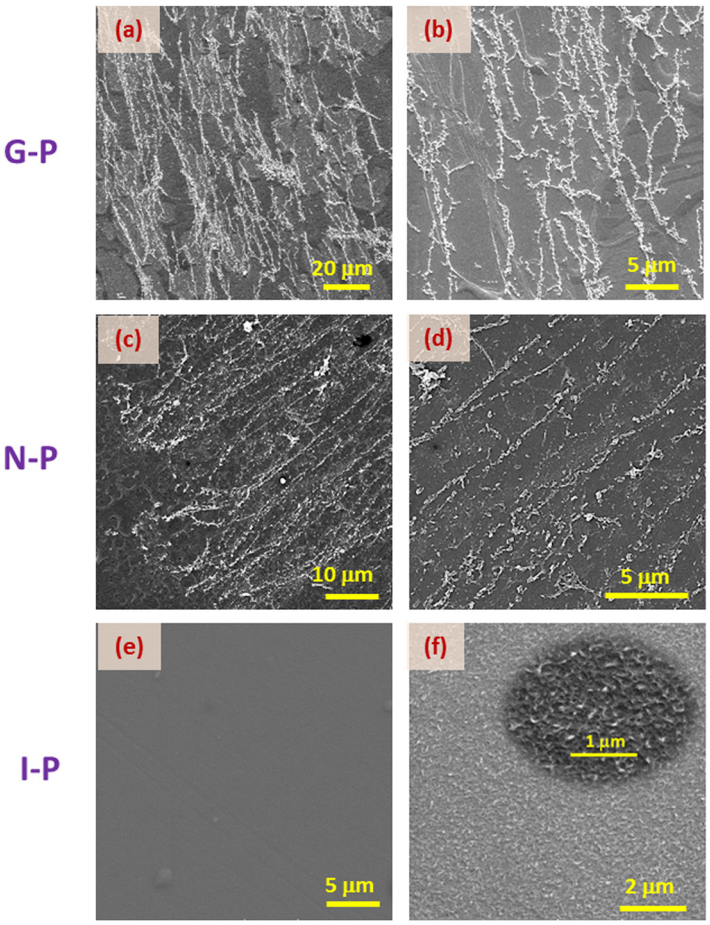

Fig. 5 SEM images depicting the polymer networks for X_{RM} = 1.75 with magnifications, (a) 1 × 10^3, (b) 5 × 10, (c) 2.5 × 10^3, (d) 7.5 × 10^3, (e) 5 × 10^3, (f) 15 × 10^3 for G-P, N-P and I-P samples shown from top to bottom, respectively. Inset in (f) showcases the short polymer strands at a higher magnification of 30 × 10^3.

value of X_{RM}, the more would be the number of nucleation centres increasing the density of the network, a feature that is reflected in Fig. 4 and 5. Besides, the magnitude of nucleation centres also decides the extent of heterogeneity of the structure: the higher the concentration of RM, the more heterogeneity of the structure.

Porosity calculation. In these systems, a necessity for obtaining high-quality SEM images is to leach out the liquid crystal after polymerization, a step required to avoid damage due to the electron beam radiation. This process retains the polymer strands in place but leads to the creation of voids or pores in regions occupied by the non-reactive LC and gelator. Removal of these components should, in principle, result in a xerogel-like situation. This problem is, however, alleviated owing to the support provided by the substrate, and thus, any change in the porosity of the system may not be expected. Image processing and analysis of the SEM images were performed using ImageJ, an open-source image processing toolbox. The not-so-well-defined boundaries prevented the software from automatically identifying the border between the polymer and the void, requiring the borders to be drawn manually. In fact, this exercise was even more tedious for the lower concentration (X_{RM} = 1.75) system. Therefore we have limited the discussion to the X_{RM} = 3 system that was only imaged at a magnification of 500 (see the scale bar in Fig. 4(a) and (e)). From Fig. 4, it is visually evident that the nematic polymerised sample has a larger void size than the gel polymerised sample. This is indeed borne out to be true from the values obtained from the image analysis carried out by calculating the geometric average over 40 counts and yielding void sizes of 36 μm and 112 μm for the G-P and N-P samples, respectively. The detailed porosity size distribution for the N-P and G-P cases is shown in Fig. 6, indicating that the G-P case has a narrower distribution than the N-P case. To arrive at quantitative differences, we fitted the histogram to a Gaussian expression. The centroid and the full-width-at-half-maximum (FWHM) values obtained from the fits are 37 ± 0.84 μm, 24.7 ± 2.8 μm for the G-P sample, and 109 ± 10.1 μm 83.6 ± 32.2 μm, for the N-P sample; the centroid values agreed (within the error bars) with the geometric average values mentioned above.

Let us recall that when the polymerization takes place, the environment is completely fluid in the case of N-P samples, but is interspersed with a gel network in the G-P case. It is tempting to consider that the already-formed gel network

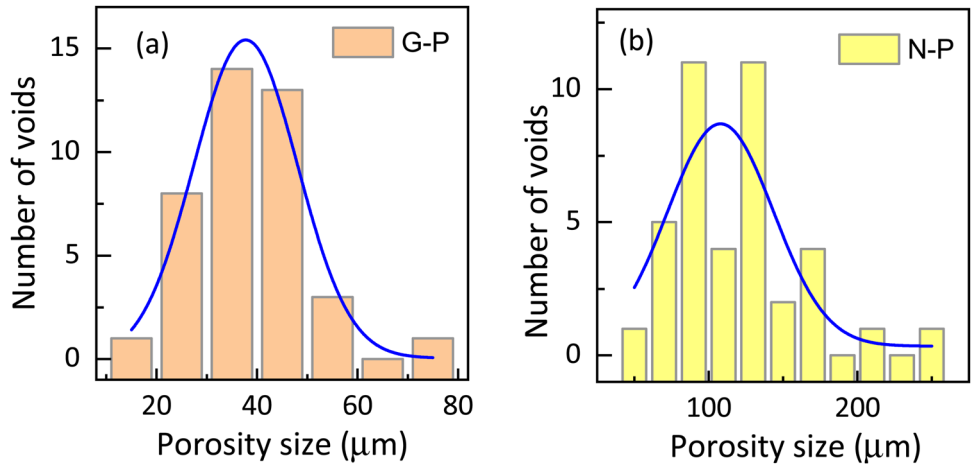

Fig. 6 Histogram showing the porosity size distribution in (a) gel-polymerized and (b) nematic polymerized samples (calculated from the SEM) images shown in Fig. 4(a) and (e). It should be noted that the horizontal scale is significantly different.

serves as a template over which the polymerization takes place. It may be mentioned that whether there is a chemical favour between the gelated HSA molecules and the RM82 monomers, is not evident. However, from the images, it is seen that the G-P case has thicker fibres compared to the N-P case. In fact, the width of the fibres averaged over the measurements at several points yields values of 0.26 μm and 0.12 μm for G-P and N-P cases. This 2-fold increase in the width perhaps is suggestive of the feature that the gel network, being a more solid platform than the fluid LC regions, favours the RM82 monomers to settle down during polymerization making the fibres thicker. Alternatively, the gel network could also be reducing the thermal fluctuation in the medium causing the formation of thicker fibres. In addition, during polymerization, the gel network reduces the volume available for the liquid crystal sample leading to a much narrower distribution of the void sizes for the G-P sample.

Fractal dimension. Determining the fractal dimension has been found as an important tool to describe a complex system.[40] As the term 'fractal' means broken or fragmented, any complex structure can exhibit self-similarity over a range of scales. Here, the self-similarity is not in the exact sense, but rather in a statistical manner. Such self-similarity is mathematically described in terms of a fractal dimension D_f, which by definition is "the exponent of the number of self-similar pieces (N) with magnification factor ($1/d$) into which a figure may be broken.[41]" The parameter D_f provides a correlation between the microscopic structure and the macroscopic properties of the system. For example, the dimensional analysis gives information about the growth mechanisms in the interfaces of physical systems, colloidal aggregation, bacterial colonies, polymer networks, *etc.* [see *e.g.*, ref. 42 and 43], with D_f characterizing the complexity of the fractal structures.[4,43] Thus, D_f indicates the irregularity of the structure and the space not occupied by the network. Especially in porous media, the fractal dimension parameter is employed to characterize the distribution of the pore/particle size and the roughness of the porous surface.[44] In 2-D, D_f varies between 1 and 2, the limits being defined for a line and a plane. Generally, a larger fractal dimension implies greater complexity involved in the objects studied.

Although the dimensionality can be calculated by various methods, we have used the standard box-counting method, implemented through the open-source software, ImageJ. The method is based on splitting the image into boxes of increasingly smaller size (d), and applying the counting protocol at each box size. Then, the relation connecting N, the number of boxes at each scale, the box size d, and the fractal dimension D_f is given by

$$D_f = \frac{\log(N)}{\log(d)} \quad (2)$$

A representation of N *vs.* d in a double logarithmic scale should yield a straight line, the slope of which gives the fractal dimension D_f (for example, see Fig. S3, ESI†). To allow unambiguous determination of the box size and subsequent calculation of the fractal dimension, the images were binarized by converting the grey image into a representation consisting of only black (pixel value = 0) and white (pixel value = 255) pixels by fixing the threshold at the half-way mark of 127. Further details, including confirmation of the analysis protocol with automatic and manual threshold values, and comparison with a literature example, are provided in ESI† under the section Fractal dimension analysis, and Fig. S4 and S5 (ESI†). As shown in Fig. 7 and 8, the binarization appears to be quite faithful for both N-P and G-P samples at coarse as well as fine scales.

Following standard practices,[40,45–47] we calculated the fractal dimension for different magnifications ranging from 100 to 20×10^3, and the results are shown in Fig. 9(a). The measured range of D_f values (1.55 to 1.8) are in agreement with others for the PSLC systems.[4,43,48] Besides, these values are also in the range seen when the mechanism is diffusion-limited cluster aggregation rather than reaction-limited cluster aggregation.[49]

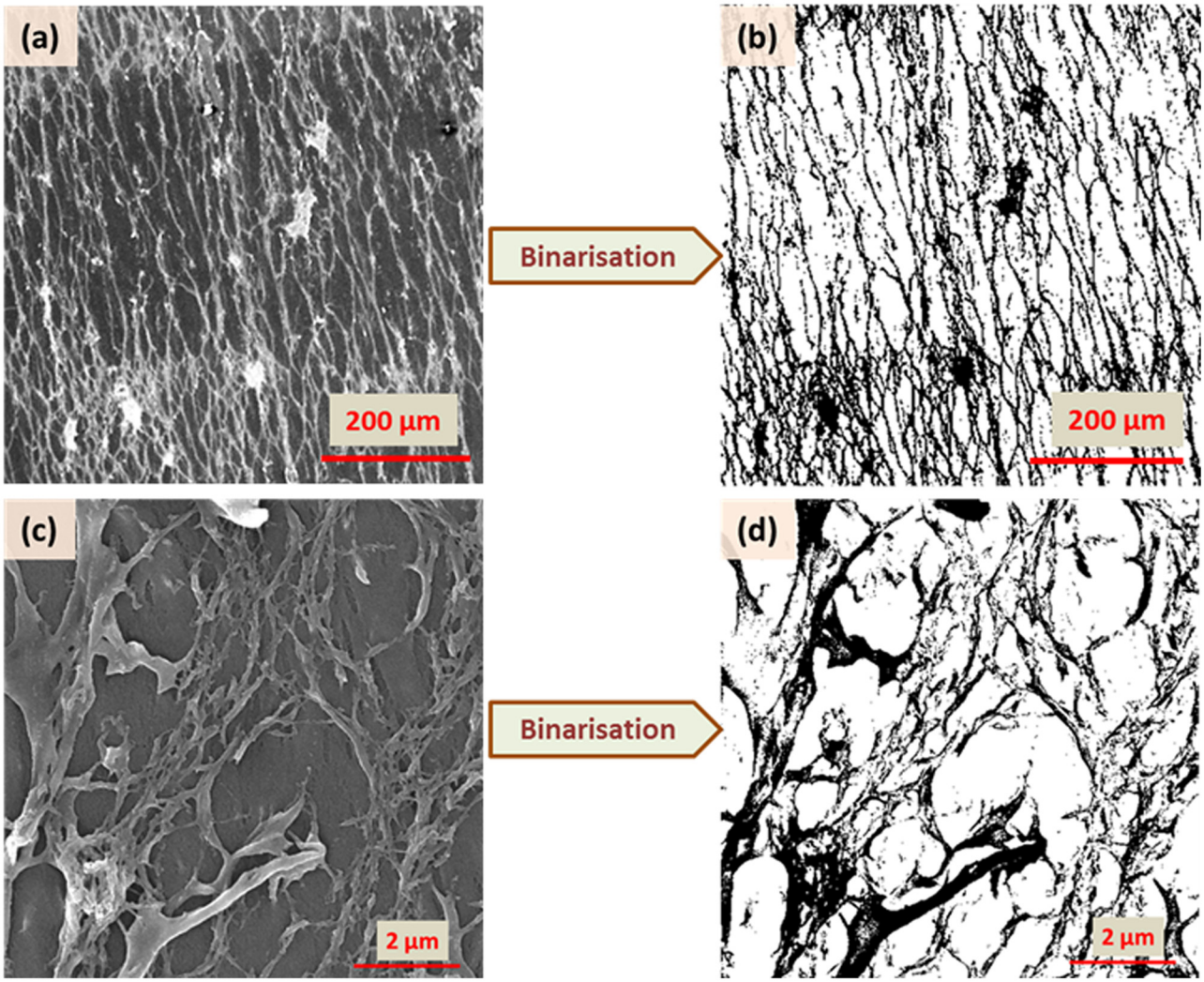

Fig. 7 Binarisation of the SEM images for X_{RM} = 3 in two different magnifications (125 and 15 × 10^3) for the N-P case.

As expected for the former mechanism, the morphology is more open. It is interesting to note that for all the magnifications used, D_f turned out to be higher for the N-P sample than for the G-P sample. The fact that D_f is expected to be a measure of the complexity of the structure, the above result should suggest that the structure is more complex for the N-P sample than for the G-P case, contrary to the visual appearance as seen in Fig. 7 and 8. Furthermore, Dierking[43] showed that the polymer curing performed at higher temperatures resulted in reduced D_f values for the formed networks. Considering that the gelation occurs at a temperature much below the isotropic-nematic point, the presently studied system has the opposite behaviour with the G-P sample having a lower D_f value.

A trivial difference that could be the reason for the opposite behaviour is that the case in ref. 43 discusses a single network system, unlike hierarchical networks in our case. More importantly, branching of the network has been proposed as a control parameter for D_f, with lower branching leading to higher fractal dimensionality.[38] As evidently observed in the SEM images, the N-P case has straighter and oriented polymer fibres resulting in lower branching, causing D_f to be higher. It is possible that in the case studied here, the branching mechanism is more dominant than the thermal effect. This viewpoint is further confirmed by the fact that as shown in Fig. 9(a), the D_f values for the G-P and N-P situations approach each other as the magnification is increased, or in other words the probing was performed on much smaller length scales, which should reduce the branching effect. In fact, it is interesting to note that in the G-P sample, the rate at which D_f increases towards the saturated value at higher magnifications, unlike the N-P case, which seems to be independent of the magnification.

As stated earlier, if the fractal dimension is indeed a robust measure of the complexity of the structure,[47] then, as the magnification increases, the complexity decreases for the G-P case but increases for the N-P sample, although the effect is much less for the latter. The voids or the porous network becoming more lucid at higher magnifications could also be the reason for this. We should hasten to add that the values for the two samples asymptotically reach a single value, which is indicative of their similar morphology at highly local

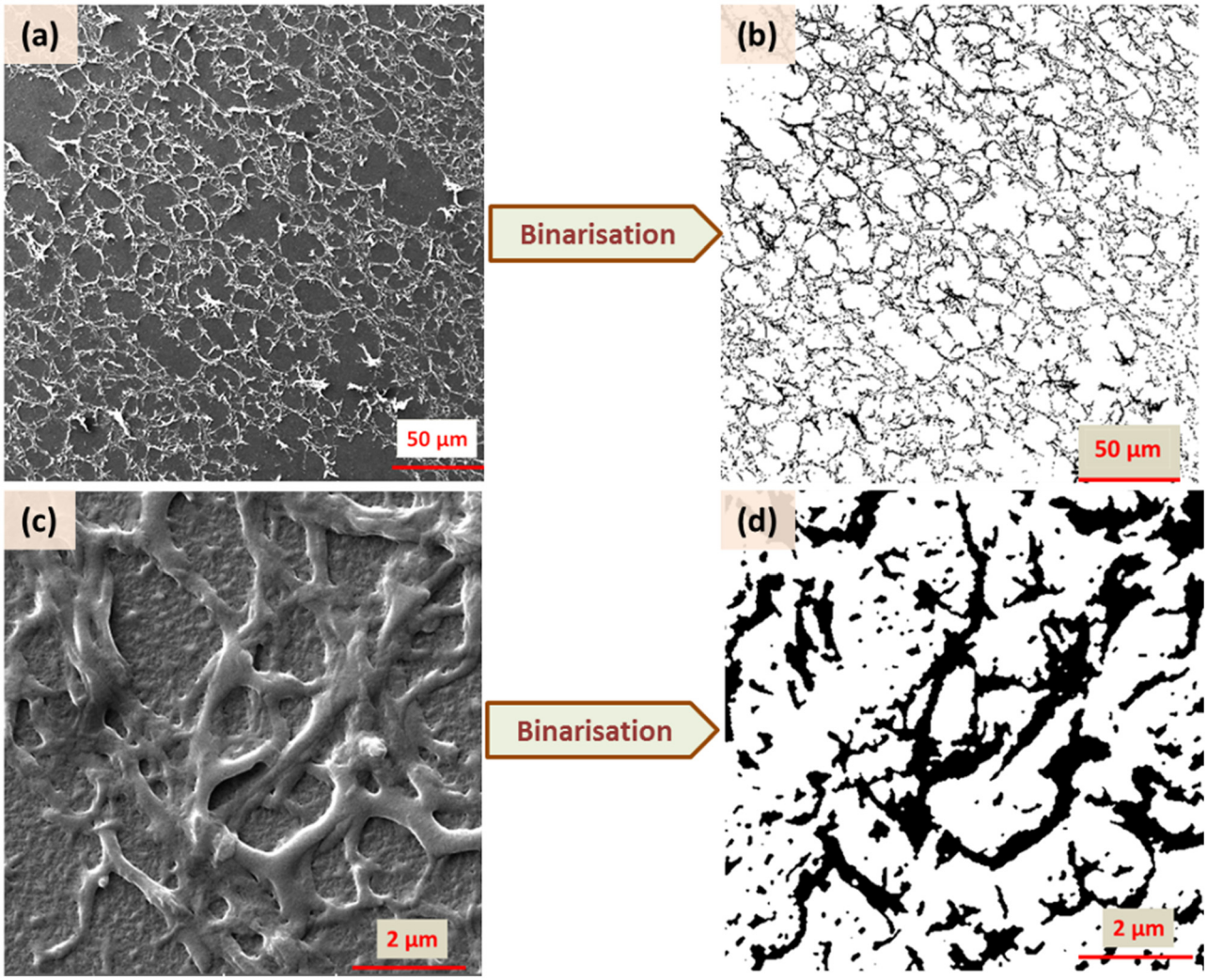

Fig. 8 Binarisation of the SEM images for X_{RM} = 3 in two different magnifications (500 and 20 × 10^3) for the G-P case.

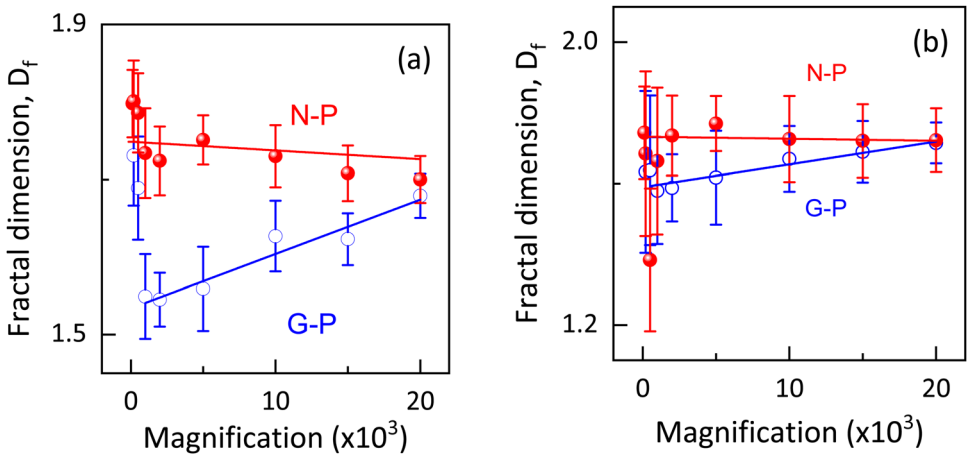

Fig. 9 Variation of fractal dimension D_f at different magnifications for N-P and G-P samples by open source software (a) ImageJ and (b) Fractalyse. In both tools, higher D_f is exhibited by the N-P compared to the G-P samples for all magnifications.

(very small length scale) levels. We could interpret that on such a small scale, complexity in the structures/formation of the polymer networks occurs more or less in a similar fashion regardless of the polymerizing temperature. The weak

magnification-dependence of D_f for the N-P case reveals better homogeneity of the networks formed.[43] Owing to the complexity and the ability to characterize an image, there are reports suggesting that the D_f values could sometimes be quite different depending on the software employed for the analyses.[50] In order to confirm the analyses performed using ImageJ, we utilised another open-source tool- 'Fractalyse' for extracting the fractal dimensionality. Not only are the D_f values from both the software agree well, but features like the trend of N-P showing higher dimensionality than G-P, and values for both N-P and G-P becoming similar at high magnifications, are also confirmed, as indeed seen in Fig. 9(b). A point to be noted is that the software generated error bar for D_f is quite high in Fractalyse as against that from ImageJ, obtained from the straight line fit (see Fig. 9); the protocol used for error calculation by Fractalyse is not known. A more detailed and controlled investigation towards these aspects with regards to the number of nucleation centres available and temperature of polymerisation is to be carried out in order to obtain better clarity about the morphological changes and the pattern formation. Further studies are also required to establish the fact that the branching is the more important parameter than the temperature in fixing the D_f values in such hierarchical networks. Apart from the regular box counting method, we have also carried out fractal dimension dependency on the grid rotation/rotation angle of the image through a process termed as 'modified box counting method'. This procedure for asymmetric images is known to exhibit an initial decrease in the value of D_f and an increase further on.[51] Similar behaviour is showcased by the G-P sample, as shown in Fig. S6 (ESI†). It is interesting to note that the variation with rotation angle is quite small and the minimum value agrees (within errors) with that from the regular box counting method as shown in Fig. 9.

3.2 Effect on gelation temperature

As stated in the introduction section, for samples thinner than a critical value, the sol–gel temperature (T_{sg}) has been seen to be strongly dependent on the sample thickness.[15] Presuming that such a feature could be arising owing to confined geometry features, we looked at the effect on T_{sg} caused by the presence of the polymer strands. The thermal variation of the transmitted laser intensity, employed to determine T_{sg} is shown in Fig. 10(a–c) for a representative concentration, X_{RM} = 1. The nematic to isotropic transition is marked by a strong change in the transmitted laser intensity (I_{laser}), the midpoint of which is taken as T_{NI}, the N–I transition temperature.

The T_{NI} values are seen to be marginally affected (<1 K) by the temperature at which the polymerization is performed or by the concentration of the polymer, X_{RM} (see Fig. S7, ESI†). In contrast, gelation is marked by a step-like reduction in I_{laser}, the step height being maximum for the G-P sample and least for the I-P sample. To avoid problems with the weak variations in the latter case, the gelation temperature was obtained as the peak point of the first differential of the data (I_{laser} *vs.* T). Even at a qualitative level, it is clear from Fig. 10(a–c) that T_{sg} is significantly dependent on the temperature at which the polymerization was performed. Similar experiments were performed by varying the polymer content, and the T_{sg} values obtained as a function of X_{RM} for the G-P, N-P, and I-P samples are shown in Fig. 10(d), (e), (f), respectively. While for all the situations T_{sg} is non-monotonic with X_{RM}, its behaviour is simpler for the I-P case. On the other hand, the N-P and G-P cases show more complicated behaviour, as evident from Fig. 10(d) and (e). Since the transition temperature exhibiting a non-monotonic change with the concentration of the dopant has been observed earlier, for example, in aerosil/LC composites, a case wherein restricted geometry effects are argued to play a significant influence, we discuss it as follows. Aerosil particles are siloyl spheres of 7 nm diameter and have a surface decoration of OH groups. When dispersed in a suitable liquid medium, including liquid crystals, the particles form a hydrogen-bonded network amongst themselves. The created 3D cage-like thixotropic structure imposes a finite-size confinement effect as well as the random-field effect on the involved phase transitions of the liquid (or LC) medium. Such an influence has been studied on the N–I, smectic, and reentrant nematic phase transitions, and even rotator phases.[52–58] For example, with octyl/octyloxy cyanobiphenyl as the LC, Roshi *et al.*[59] found that a high degree of non-monotonicity existed in the transition temperatures as the aerosil concentration was increased, with the maximum downward deviation of 1–2 °C for a concentration of $\sim$10% aerosil particles. In light of these observations, it may be noted that the deviations observed for the sol–gel transition in the present case of polymer confinement are much larger, despite the concentrations of the dopant (X_{RM}) being much smaller.

A point that must be borne in mind, however, is that a direct comparison between the type of network formation in the present scenario and the LC + aerosil mixture may not be appropriate. Although, in both cases, networking is due to weak hydrogen bonding, the key difference is in the nature of the gel formation. In the aerosil case, it is the silica spheres that hydrogen bond together to form a random irreversible gel, whereas in the present case, HSA molecules undergo a completely reversible sol–gel process. Additionally, when present, the polymerized network acts as a template for creating further confinement of the HSA molecules. The existence of the orientational order in both the N-P and G-P cases adds further dimensionality. In fact, Sharma[60] reported that in LC + aerosil mixtures the calorimetric parameters differ between the (LC) oriented and un-oriented cases. It was also noted that in aligned LC hosts, aerosil gels are stiffer due to increased surface interaction between the aerosil and LC molecules, resulting in changes associated with enthalpy and transition temperatures. On similar lines, for the present case, when polymer strands are existing (N-P and G-P case), the hydrogen bonding of the HSA molecules will be assisted by the cage of RM82 networks. The non-monotonic variations in T_{sg} could be a combined result of the number of HSA molecules available to form hydrogen bonds and the alignment of polymer strands. In contrast, for the I-P case, the development of gel fibres is least affected as the polymer network formed is disconnected to the maximum extent, a fact supported by POM and SEM images.

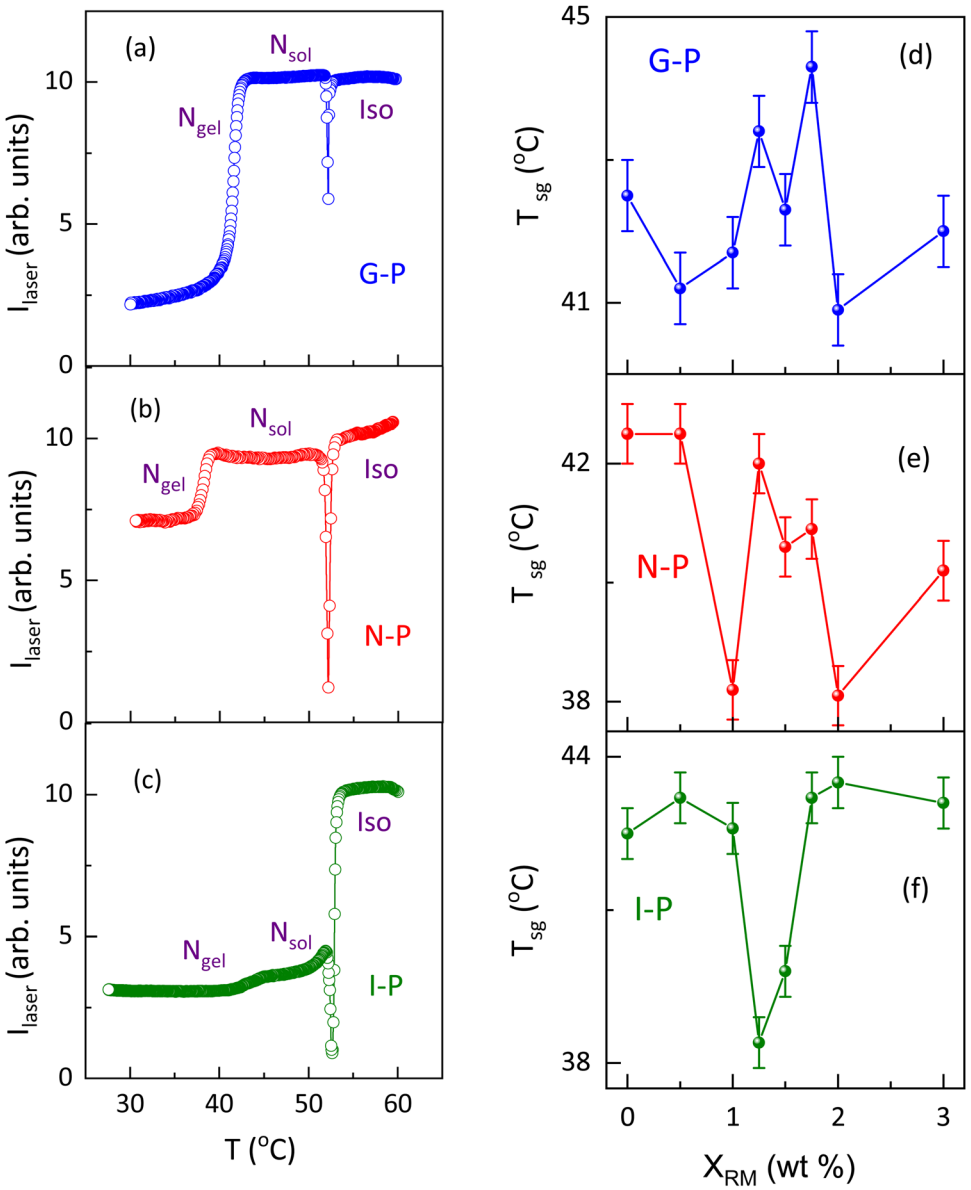

Fig. 10 Thermal variation of transmitted laser intensity (I_{laser}) for the G-P, N-P, and I-P cases, for X_{RM} = 1 in (a), (b), (c) respectively. The variation of T_{sg} with different X_{RM} is shown for the G-P, N-P, and I-P cases in (d), (e), (f), respectively.

The higher complexity of the networks involved and their mutual interactions could also be the reasons for the non-trivial behaviour of the T_{sg} on the polymerization temperature as well as with the variation of X_{RM}. In a study of coexisting physical networks of self-assembled fibrillar networks (SAFINs) and self-assembled micellar networks (SAMINs), it has been comprehended that the mutual influence of the network rules the mechanical properties and thereby the network integrity and various other parameters in these organogels.[39] It has also been stated that the presence of one network and the temperature at which it is forming either trigger or hinder the formation of a second network.[39] Although, at present, we are not able to explain the non-monotonicity in T_{sg}, we can contemplate that the changes in gelation temperatures could be a combination of factors such as the monomer concentration and the temperature of polymerization, which in turn decides the hierarchy of the network to be formed. For instance, in the I-P case, the gel fibres could be formed without much challenge posed by the polymerized environment and hence T_{sg} is least affected (see Fig. 10(f)). On the other hand, in the N-P case, polymer strands are formed in correlation with the LC orientations. Hence, as X_{RM} increases, dense, well-oriented, stronger strands are formed, which pose a more significant challenge for the weak gel fibers to form hydrogen bonding and gelate, resulting in complex behaviour of the gelation temperature shown in Fig. 10(e). Similarly, for the G-P case, the polymerization occurs in the presence of the gel fibre network yielding random polymer networks. Also, it should be noted that for all X_{RM}, the deviation in T_{sg} is with respect to the X_{RM} = 0 system. A point to be noted, especially in the N-P case, is that, once the

Table 1 A summary of the effect of polymerization at different temperatures

Type of polymerisation parameters	Gel polymerised (G-P) (30 °C)	Nematic polymerised (N-P) (50 °C)	Isotropic polymerised (I-P) (60 °C)
Environment	Nematic oriented gel fibres	Oriented NLC without gel fibres	No orientation either for NLC or gel fibres
Influence on polymerisation	Influenced by the network of existing gel fibres leading to not so oriented polymer networks	Solely influenced by NLC orientation leading to well aligned polymer strands	Random polymerisation leading to weak/short polymer strands
Impact on gelation temperature (T_{sg})	Complex Already gel fibres were present during polymerisation	Complex Existing well aligned polymer strands challenge the growth of gel fibres in the nematic environment	Simple As weak/short polymer strands are formed, it reduces the restrictions for gel formation

polymerization is performed it can be expected that several HSA molecules get trapped inside the polymer fibre and thus in the subsequent thermal cycles, lack the freedom to participate in the gelation process. This should effectively diminish the concentration of the gelator.

Another competing feature that can result due to the oriented polymer fibres formed in the N-P case is that a few HSA molecules present near the polymer fibre walls will have reduced thermal fluctuations and thus have a favour for better hydrogen bonding amongst themselves. This will in turn increase the sol–gel temperature. In all three cases, a feature that is invariably present is the reduced space available for the gel fibres to form, the reduction monotonically increasing with X_{RM}. Thus, T_{sg} was determined by a combination of several of these factors. An overview of the impact of gelation temperature and its influence on polymerization due to temperature is tabulated in Table 1. Fig. 11 is a schematic overview of polymerization under the three conditions.

3.3 Smart window application

Encouraged by the visual appearance of the sample cells formed under the three conditions, we contemplated fabricating a smart window application that worked on the following principle. Normally, a nematic polymerised PSLC device operates from a transparent to a scattering state on the application of voltage. But we can reverse this behaviour when polymerised in the isotropic phase. The I-P samples operated in a scattering state, which when sufficient voltage was applied became transparent as can be visualised from Fig. 12(a). Such devices have been proposed to be the next-generation solution for low-energy consuming dwellings, privacy windows, *etc.*[23,61] An essential parameter considered for fabrication of such a

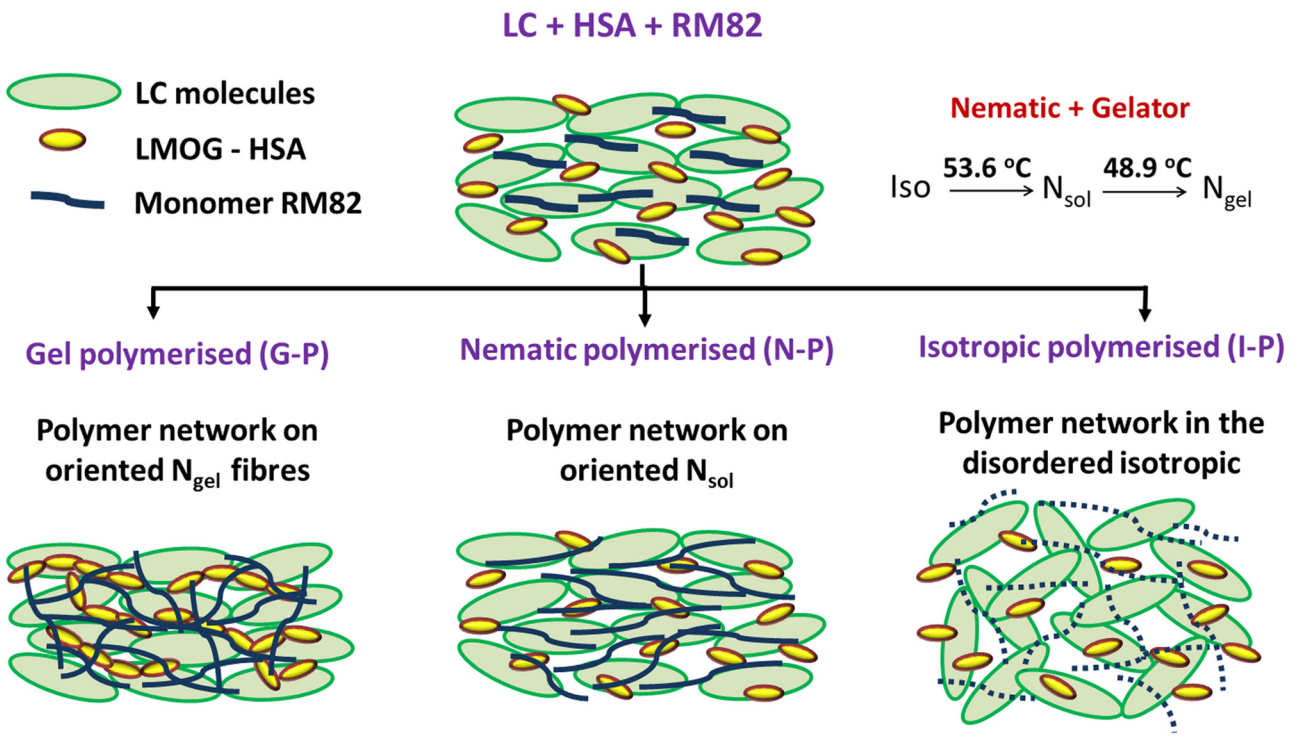

Fig. 11 Schematic of the network formation when polymerized in 3 different phases.

window in the equilibrium (no-voltage) state is the haze, defined as the amount of light scattered by the sample. The required spectroscopic measurements were performed over the entire visible region employing the methodology summarized in Fig. S2 (ESI†), and the haze factor was calculated using eqn (1). The spectra determined for samples X_{RM} = 1 and 3 under the three polymerization conditions are presented in Fig. 12(b) and (c). Apart from the overall haze factor being higher for X_{RM} = 3 than for X_{RM} = 1 mixture, surprisingly, the I-P samples have higher haze values than their N-P or G-P counterparts. Increased scattering for X_{RM} = 3 can be explained based on the density of the polymer fibres present: the denser the network, the higher the scattering ability. Meanwhile, increased haze for I-P is the consequence of the larger population of short fibres having no orientational order in the isotropic environment. This randomness in the network, associated with the mismatch in the refractive indices of the LC and RM82 regions is the key reason for the increased scattering. Hence, from a device fabrication point of view, it may be said that it is ideal to polymerize in the isotropic phase, although we agree that there is much room for improving its scattering ability. We believe that a careful interplay of monomer and gelator concentrations can bring out this aspect in a more refined way. Visual evidence of these features is well brought out in the images of the devices with the I-P sample having the highest scattering (Fig. 12(a)).

3.4 Electric behaviour

Temperature-dependent permittivity. The thermal variations of the low-frequency (1 kHz) permittivity, along ($\varepsilon_{\parallel}$) and perpendicular ($\varepsilon_{\perp}$) to the nematic director for the G-P, N-P, and I-P cases are shown in Fig. S8(a)–(c) (ESI†), respectively. Permittivity changes are quite small across the N_{sol}–N_{gel} transition for all three cases of polymerization. The orientational aspects of the polymer networks play a major role in their contribution to the permittivity. In fact, it is evident from Fig. S8 (ESI†) that the contribution to $\varepsilon_{\parallel}$ decreases as X_{RM} increases. For measuring $\varepsilon_{\parallel}$, an AC voltage (20 V) is applied to reorient the LC molecules from their equilibrium planar orientation denser networks at higher polymer content that poses more challenges for the LC molecules to reorient. Indeed, the effect of polymerising at different temperatures is also apparent as seen in Fig. S8 (ESI†). G-P samples are the most affected ones with I-P being the least. Once again, the morphology of the

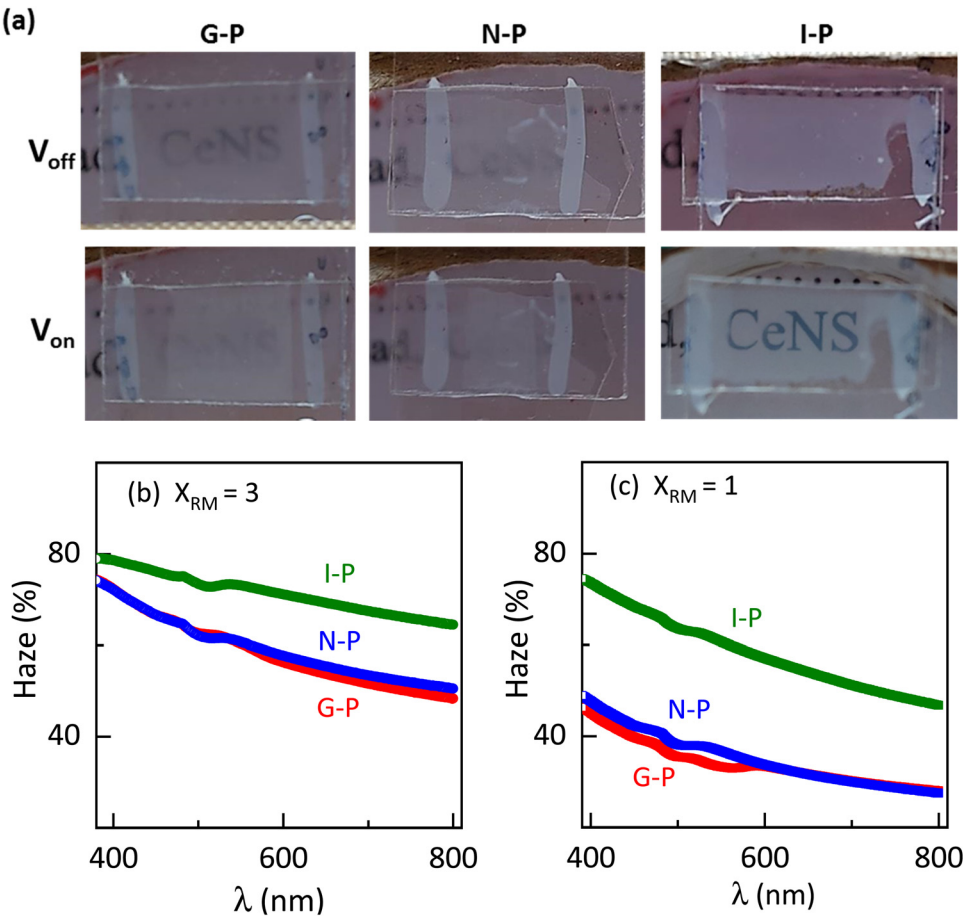

Fig. 12 (a) Images of light scattered by G-P, N-P, and I-P at room temperature for X_{RM} = 3. Visually, we can observe higher haze for the I-P sample. Haze measured in the visible region for (b) X_{RM} = 3 and (c) X_{RM} = 1. Higher haze is exhibited for X_{RM} = 3. I-P samples scatter more light compared to G-P and N-P for both X_{RM} = 3 and 1.

networks formed is crucial, which also determines the contribution to the permittivity of the system.

Electric field-driven Freedericksz transition. Fig. S9 (ESI†) shows raw profiles of voltage dependence of the permittivity for X_{RM} = 1.5 for the G-P case, at two different temperatures depicting nematic sol (50 °C) and nematic gel (30 °C) phases. It is clearly seen from the inset of Fig. S9 (ESI†) that the threshold voltage V_{th}, is higher in the gel phase, apparently caused by lower thermal fluctuations, the associated higher order parameter, and the presence of the second network. Table S1 (ESI†) represents the concentration dependence of threshold voltage at 50 °C and 30 °C. The variation with X_{RM} is non-monotonic, however, the extent of change in V_{th} is minimal ($\sim$0.2 V), for all three cases.

Splay elastic constant. The Freedericksz transformation data were employed to calculate the splay elastic constant through eqn (3).

$$K_{11} = \frac{\varepsilon_0 \varepsilon_a {v_{th}}^2}{\pi^2} \quad (3)$$

Here ε_0 is the permittivity of free space and $\varepsilon_a = (\varepsilon_{\parallel} - \varepsilon_{\perp})$, the dielectric anisotropy. The variation of the splay elastic constant is shown in Table S2 (ESI†) for 50 °C and 30 °C. As expected, K_{11} also follows the trend of V_{th} variation. Although it is quite challenging to understand the trend of concentration dependence, we could see that the values in the nematic gel phase, *i.e.*, at 30 °C, values are higher when compared to those in the nematic phase. The gel networks formed along with reduced thermal fluctuations hinder the reorientation of LC molecules resulting in the increase of splay elastic constant, K_{11}. The observed highly non-monotonic behaviour of the V_{th} and K_{11} as a function of X_{RM}, especially for intermediate concentrations, resembling the T_{sg} variation implies that further investigations are required to understand these systems in more detail.

Switching dynamics. For investigating the dynamics of electro-optic switching, the sample was kept between crossed polarizers, and the intensity of the transmitted light beam was collected using a photo-diode and the associated electronics. For a representative mixture, X_{RM} = 2 polymerized in the gel phase, the photo-diode responses in the field on and off situations are shown in Fig. S9(a) (ESI†) at two temperatures corresponding to the gel (30 °C) and N phases (50 °C). Similar data for the same mixture, but polymerized in the isotropic phase, are shown in Fig. S8(b) (ESI†). To determine the dynamics quantitatively, the response time τ_{ON} is defined as the time required for the transmission to change, upon turning the field on, from 10% to 90% of the saturated intensity, and τ_{OFF} is the time taken for the transmission to reduce from 90% to 10% of the saturated intensity value. A well-known fact in LCs and LCGs is that generally, τ_{OFF} timescales are higher than τ_{ON}, which holds true for the present case as well. Also, it is seen that switching a nematic phase is easier than switching a gel phase (which can be corroborated by the response curve). Consequently, the response times are higher in the gel phase compared to the nematic phase. The response times for all the I-P, N-P, and G-P cases for different X_{RM} mixtures are presented in Table S3 (ESI†).

4. Summary

We have carried out investigations by employing two networks formed through polymer and gelator in an anisotropic nematic host. Temperature (or mesophase) dependent polymerization is involved, which helped us in realizing the impact of liquid crystal orientation on the networks being formed and their mutual influences as well. Increased arbitrariness was observed for the gel polymerized samples compared to nematic and isotropic polymerized samples, which are corroborated by detailed morphological investigations using POM and SEM characterizations. The SEM image analysis reveals that the N-P sample exhibited 3 times larger porosity compared to the G-P sample, indicating the amount of LC trapped between the polymer networks. Fractal dimension, D_f indicates more complexity shown by N-P samples in comparison with the G-P case. The gelation temperature varies in a non-monotonic fashion with the concentration of the monomer. It is observed that the impact on the gelation temperature is more for N-P samples, intermediate for G-P, and least for I-P samples directing towards the formation of hierarchical networks. Haze measurement indicated that the I-P sample demonstrates better scattering ability compared to G-P and N-P samples. The observed features were explained based on the hierarchy of the two physical networks-polymer and gel networks formed and their mutual interaction. We believe that these experiments comprise double networks in liquid crystals and have paved a distinct approach in the field of LC research.

Conflicts of interest

There are no conflicts of interest to declare.

Acknowledgements

Dr D. S. Shankar Rao and Dr S. Krishna Prasad acknowledge the funding support from a SERB project numbered CRG/2019/001671.

References

1 S. Dutta and S. Krishna Prasad, *Phys. Chem. Chem. Phys.*, 2018, **20**, 24345–24352.
2 M. Vijay Kumar, S. Krishna Prasad, D. S. Shankar Rao and E. P. Pozhidaev, *Phase Trans.*, 2013, **86**, 323–338.
3 M. Mizukami, N. Ohta, K. Tomita, T. Yanagimachi, Y. Shibuya, N. Yagi and K. Kurihara, *Phys. Chem. Chem. Phys.*, 2021, **23**, 131–138.
4 I. Dierking, *Polymer-modified Liquid Crystals*, Royal Society of Chemistry, UK, 2019.
5 Y. K. Fung, D. K. Yang, S. Ying, L. C. Chien, S. Zumer and J. W. Doane, *Liq. Cryst.*, 1995, **19**, 797–801.

6 T. Kato, Y. Hirai, S. Nakaso and M. Moriyama, *Chem. Soc. Rev.*, 2007, **36**, 1857–1867.
7 Y. G. Marinov, G. B. Hadjichristov, A. G. Petrov and S. K. Prasad, *Composites, Part B*, 2016, **90**, 471–477.
8 J. Leys, C. Glorieux and J. Thoen, *J. Non. Cryst. Solids*, 2010, **356**, 597–601.
9 T. Kato, J. Uchida, T. Ichikawa and T. Sakamoto, *Angew. Chem., Int. Ed.*, 2018, **57**, 4355–4371.
10 Z. Wei, Y. Deng, M. Yu and H. Yu, *Liq. Cryst.*, 2020, **47**, 1170–1179.
11 Y. Ni, X. Li, J. Hu, S. Huang and H. Yu, *Chem. Mater.*, 2019, **31**, 3388–3394.
12 V. V. Mohanan, B. Pradhan, V. Sridurai, C. V. Yelamaggad, A. S. Achalkumar and G. G. Nair, *Nanoscale*, 2018, **10**, 15686–15695.
13 S. Vimala, S. M. Sathya, G. G. Nair, S. K. Prasad and C. V. Yelamaggad, *J. Mater. Chem. C*, 2016, **4**, 11313–11320.
14 H. Shahsavan, A. Aghakhani, H. Zeng, Y. Guo, Z. S. Davidson, A. Priimagi and M. Sitti, *Proc. Natl. Acad. Sci. U. S. A.*, 2020, **117**, 5125–5133.
15 G. V. Varshini, S. Parthasarathi, D. S. Shankar Rao and S. Krishna Prasad, *Soft Matter*, 2022, **18**, 8792–8803.
16 I. Dierking, *Polym. Chem.*, 2010, **1**, 1153–1159.
17 D. S. Hou, L. Zheng, D. P. Sun, X. Zhou, J. L. Zhu and W. M. Han, *Liq. Cryst.*, 2021, **49**, 201–208.
18 A. V. Kaznacheev, E. P. Pozhidaev, S. I. Torgova, V. A. Barbashov and V. V. Kesaev, *Opt. Mater. Express*, 2020, **10**, 3030–3040.
19 M. H. Saeed, S. Zhang, Y. Cao, L. Zhou, J. Hu, I. Muhammad, J. Xiao, L. Zhang and H. Yang, *Molecules*, 2020, **25**, 5510.
20 Y. Zhang, C. Wang, W. Zhao, M. Li, X. Wang, X. Yang, X. Hu, D. Yuan, W. Yang, P. Lv, J. He and G. Zhou, *Polymer*, 2019, **11**, 1869.
21 N. Nasir, H. Hong, M. A. Rehman, S. Kumar and Y. Seo, *RSC Adv.*, 2020, **10**, 32225–32231.
22 B. Kamaliya, M. Vijay Kumar, C. V. Yelamaggad and S. Krishna Prasad, *Appl. Phys. Lett.*, 2015, **106**, 083110.
23 S. Krishna Prasad, M. Baral, A. Murali and S. N. Jaisankar, *ACS Appl. Mater. Interfaces*, 2017, **9**, 26622–26629.
24 P. L. Madhuri, S. K. Prasad and G. G. Nair, *RSC Adv.*, 2014, **4**, 3121–3130.
25 J. P. Gong, Y. Katsuyama, T. Kurokawa and Y. Osada, *Adv. Mater.*, 2003, **15**, 1155–1158.
26 E. S. Dragan, *Pure Appl. Chem.*, 2014, **86**, 1707–1721.
27 S. Ishikawa, K. Iijima, D. Matsukuma, Y. Asawa, K. Hoshi, S. Osawa and H. Otsuka, *Chem. Mater.*, 2020, **32**, 2353–2364.
28 A. A. Aldana, S. Houben, L. Moroni, M. B. Baker and L. M. Pitet, *ACS Biomater. Sci. Eng.*, 2021, **7**, 4077–4101.
29 N. Raina, R. Rani, A. Khan, K. Nagpal and M. Gupta, *Polym. Bull.*, 2020, **77**, 5027–5050.
30 K. H. Yun, J.-C. Lee and J.-M. Seo, *J. Korean Ophthalmic. Opt. Soc.*, 2019, **24**, 109–115.
31 R. Badugu, B. H. Jeng, E. A. Reece and J. R. Lakowicz, *Anal. Biochem.*, 2018, **542**, 94.
32 S. Zhong and C. H. Jang, *Biosens. Bioelectron.*, 2014, **59**, 293–299.
33 K. G. Noh and S. Y. Park, *Adv. Funct. Mater.*, 2018, **28**, 170756.
34 Y. Hirai, N. Mizoshita, M. Moriyama and T. Kato, *Langmuir*, 2009, **25**, 8423–8427.
35 D. Yang, in *Progress in liquid crystal science and technology*, ed. H.-S. Kwok, S. Naemura and H. L. Ong, World Scientific, 2013, pp. 597–628.
36 M. Trudicova, J. Smilek, M. Kalina, M. Smilkova, K. Adamkova, K. Hrubanova, V. Krzyzanek and P. Sedlacek, *Polymer*, 2020, **12**, 2561.
37 V. Lotito and T. Zambelli, *Adv. Colloid Interface Sci.*, 2020, **284**, 102252.
38 G. M. Newbloom, P. De La Iglesia and L. D. Pozzo, *Soft Matter*, 2014, **10**, 8945–8954.
39 A. S. Krishnan, P. H. Vargantwar and R. J. Spontak, *Soft Matter*, 2012, **8**, 12025–12033.
40 A. K. Bisoi and J. Mishra, *Pattern Recognit. Lett.*, 2001, **22**, 631–637.
41 K. M. Iftekharuddin and F. Ahmed, in *Encyclopedia of Modern Optics*, ed. D. G. Steel and R. D. Guenther, Elsevier, 2005, pp. 206–218.
42 *Fractals in Science*, ed. A. Bunde and S. Havlin, Springer, Berlin, 1994.
43 I. Dierking, *J. Phys. D: Appl. Phys.*, 2002, **35**, 2520–2525.
44 Y. Xia, J. Cai and W. Wei, in *Modelling of Flow and Transport in Fractal Porous Media*, ed. J. Cai, L. Zhang and W. Wei, Elsevier, 2021, pp. 11–24.
45 I. Dierking, *Adv. Mater.*, 2003, **15**, 152–156.
46 W. Zhao, J. Yan, G. Hou, P. Diwu, T. Liu, J. Hou and R. Li, *Front. Chem.*, 2021, **9**, 732797.
47 H. P. Tang, J. Z. Wang, J. L. Zhu, Q. B. Ao, J. Y. Wang, B. J. Yang and Y. N. Li, *Powder Technol.*, 2012, **217**, 383–387.
48 P. Satapathy, S. Parthasarathi, D. S. S. Rao, S. Bano, Y. S. Negi and S. K. Prasad, *Appl. Phys. Lett.*, 2020, **117**, 103702.
49 L. Turetta and M. Lattuada, *Soft Matter*, 2022, **18**, 1715–1730.
50 E. Hadzieva, D. C. Bogatinoska, L. Gjergjeska, M. Shumi-Noska and R. Petroski, ICT Innov. 2015 Web Proc., pp. 201–211.
51 D. Ristanović, B. D. Stefanović and N. Puškaš, *Theor. Biol. Forum*, 2014, **107**, 109–121.
52 M. V. Kumar and S. K. Prasad, *RSC Adv.*, 2012, **2**, 8531–8538.
53 T. Jin and D. Finotello, *Phys. Rev. Lett.*, 2001, **86**, 818.
54 C. C. Retsch, I. McNulty and G. S. Iannacchione, *Phys. Rev. E*, 2002, **65**, 032701.
55 S. Park, R. L. Leheny, R. J. Birgeneau, J. L. Gallani, C. W. Garland and G. S. Iannacchione, *Phys. Rev. E*, 2002, **65**, 050703.
56 M. Marinelli, A. K. Ghosh and F. Mercuri, *Phys. Rev. E*, 2001, **63**, 061713.
57 B. Zhou, G. S. Iannacchione, C. W. Garland and T. Bellini, *Phys. Rev. E*, 1997, **55**, 2962.
58 G. S. Iannacchione, C. W. Garland, J. T. Mang and T. P. Rieker, *Phys. Rev. E*, 1998, **58**, 5966.
59 A. Roshi, G. S. Iannacchione, P. S. Clegg and R. J. Birgeneau, *Phys. Rev. E*, 2004, **69**, 1–11.
60 D. Sharma, *Liq. Cryst.*, 2008, **35**, 1215–1224.
61 M. Baral, K. Bramhaiah, N. S. John and S. Krishna Prasad, *ACS Omega*, 2019, **4**, 403–411.

